ADVANCES IN ATMOSPHERIC SCIENCES, VOL. 33, JANUARY 2016, 101–109

# Radiative Effects on Torrential Rainfall during the Landfall of Typhoon Fitow (2013)

Lingyun LOU and Xiaofan LI*

*School of Earth Sciences, Zhejiang University, Hangzhou* 310027

(Received 3 June 2015; revised 23 July 2015; accepted 26 July 2015)

ABSTRACT

Cloud microphysical and rainfall responses to radiative processes are examined through analysis of cloud-resolving model sensitivity experiments of Typhoon Fitow (2013) during landfall. The budget analysis shows that the increase in the mean rainfall caused by the exclusion of radiative effects of water clouds corresponds to the decrease in accretion of raindrops by cloud ice in the presence of radiative effects of ice clouds, but the rainfall is insensitive to radiative effects of water clouds in the absence of radiative effects of ice clouds. The increases in the mean rainfall resulting from the removal of radiative effects of ice clouds correspond to the enhanced net condensation. The increases (decreases) in maximum rainfall caused by the exclusion of radiative effects of water clouds in the presence (absence) of radiative effects of ice clouds, or the removal of radiative effects of ice clouds in the presence (absence) of radiative effects of water clouds, correspond mainly to the enhancements (reductions) in net condensation.

The mean rain rate is a product of rain intensity and fractional rainfall coverage. The radiation-induced difference in the mean rain rate is related to the difference in rain intensity. The radiation-induced difference in the maximum rain rate is associated with the difference in the fractional coverage of maximum rainfall.

**Key words**: radiative effects, rainfall, maximum rainfall, rain intensity, fractional rainfall coverage, net condensation, hydrometeor change

**Citation**: Lou, L. Y., and X. F. Li, 2016: Radiative effects on torrential rainfall during the landfall of Typhoon Fitow (2013). *Adv. Atmos. Sci.*, **33**(1), 101–109, doi: 10.1007/s00376-015-5139-y.

## 1. Introduction

During summer in the Northern Hemisphere, landfalling typhoons can cause severe floods along the coastal areas of eastern and southern China, resulting in regular economic loss. The rainfall during typhoon landfall is affected by various physical processes and factors. Among them, cloud radiative processes play an important role in the development and maintenance of typhoon rainfall. The clouds impact thermal stratification through the reflection of solar radiation at the top of clouds and prevention of infrared radiation escaping into space. Such a change in temperature affects the net condensation through the change in saturation specific humidity and cloud microphysical processes. The rainfall can be influenced by cloud radiative processes through the development of the secondary circulation induced by the difference in radiative heating between cloudy and clear-sky areas (Gray and Jacobson, 1977), destabilization of thermal stratification (Lilly, 1988; Dudhia, 1989), and the increase in relative humidity (Tao et al., 1993) or decrease in saturation mixing ratio (Sui et al., 1997, 1998; Gao et al., 2009; Gao and Li, 2010) in response to infrared radiative cooling.

Deep convection and torrential rainfall are often associated with the development of typhoons. The torrential rainfall during the landfall of typhoons usually leads to natural disasters such as floods and mudslides, which can cause tremendous economic and human losses. Deep convection consists of water and ice clouds, depending on the air temperature. Ice clouds are semi-transparent to solar radiation but opaque to infrared radiation, and therefore have a strong greenhouse effect. On the contrary, water clouds reflect most solar radiation back to space due to their large optical thickness, and have a dominant cooling effect. Radiative processes of water and ice clouds may impact upon the development of typhoon rainfall through the change in cloud microphysical processes. Thus, studying the radiative effects of water and ice clouds on typhoon rainfall can enhance understanding of the dominant physical processes involved, and help determine the cloud radiative effects on typhoon rainfall intensity.

The objective of this study is to separately examine the radiative effects of water and ice clouds on the cloud microphysics and rainfall associated with a typhoon, through analysis of cloud microphysical budgets with sensitivity experiments. Typhoon Fitow (2013) is selected for this purpose. Fitow (2013) strengthened to a typhoon in the early morning

* Corresponding author: Xiaofan LI
Email: xiaofanli@zju.edu.cn

of 3 October 2013 and made landfall with a maximum wind of 42 m $s^{-1}$ and minimum pressure of 955 hPa at Fuding, Fujian, at around 0115 LST (local standard time) 7 October. It weakened to a tropical storm at around 0500 LST 7 October. Fitow caused economic losses of over 10 billion US Dollars, mainly through significant floods in several cities in Zhejiang Province after its landfall in Fujian Province. Li et al. (2015) defined the model domain mean rain rate as the product of rain intensity (RI) and fractional rainfall coverage (FRC). They analyzed the diurnal variation of tropical rainfall using equilibrium cloud-resolving model simulation data and found that the diurnal variation of the mean rain rate is associated with that of FRC because the diurnal variation of RI is significantly weakened through the decrease in rainfall in the early morning hours. RI and FRC may respond to radiative processes differently. Thus, radiative effects on RI and FRC will be examined. The model, large-scale forcing, and sensitivity experiments are briefly described in section 2. The control experiment is discussed in section 3. Cloud microphysical and rainfall responses to radiative processes are examined in section 4. A summary is provided in section 5.

## 2. Model, experiments and analysis methodologies

A 2D cloud-resolving model (Soong and Ogura, 1980; Soong and Tao, 1980; Tao and Simpson, 1993; Sui et al., 1994, 1998; Li et al., 1999, 2002) is used to simulate Typhoon Fitow (2013). The model (Gao and Li, 2008; Li and Gao, 2011), with periodic boundary conditions, contains prognostic equations for perturbation momentum, potential temperature, specific humidity and five cloud species (cloud water, raindrops, cloud ice, snow and graupel). The source/sink terms in the specific humidity and cloud equations include cloud microphysical parameterization schemes (Lin et al., 1983; Rutledge and Hobbs, 1983, 1984; Tao et al., 1989; Krueger et al., 1995; also see Table 1). The source/sink terms in the thermodynamic equation include solar and infrared radiative parameterization schemes (Chou, 1992; Chou and Suarez, 1994; Chou et al., 1991, 1998).

The control experiment (CTL) is simulated with imposed large-scale forcing (Fig. 1) from 0800 LST 5 October to 0800 LST 9 October 2013. The six-hourly large-scale forcing is interpolated and imposed in the model every 12 s. The forcing is averaged in a rectangular box covering (26°–34°N, 118°–122°E) (Fig. 1) using NCEP/GDAS (National Centers for Environmental Prediction/Global Data Assimilation System) data. Figure 1 shows that the maximum rain amount during 5–9 October 2013 was over 500 mm. The forcing includes zonally uniform vertical velocity, zonal wind (Fig. 2) and horizontal temperature and vapor advection (not shown). The maximum upward motion was over 16 cm $s^{-1}$ at 6 km around midnight of 6 October 2013 (Fig. 2a), while westerly winds developed in the mid and upper troposphere and extended to the lower troposphere (Fig. 2b).

**Table 1.** List of microphysical processes and their parameterization schemes. The schemes are Lin et al. (1983) (LFO), Rutledge and Hobbs (1983, 1984) (RH83, RH84), Tao et al. (1989) (TSM), and Krueger et al. (1995) (KFLC).

| Notation | Description | Scheme |
|---|---|---|
| $P_{MLTG}$ | Growth of vapor by evaporation of liquid from graupel surface | RH84 |
| $P_{MLTS}$ | Growth of vapor by evaporation of melting snow | RH83 |
| $P_{REVP}$ | Growth of vapor by evaporation of raindrops | RH83 |
| $P_{IMLT}$ | Growth of cloud water by melting of cloud ice | RH83 |
| $P_{CND}$ | Growth of cloud water by condensation of supersaturated vapor | TSM |
| $P_{GMLT}$ | Growth of raindrops by melting of graupel | RH84 |
| $P_{SMLT}$ | Growth of raindrops by melting of snow | RH83 |
| $P_{RACI}$ | Growth of raindrops by the accretion of cloud ice | RH84 |
| $P_{RACW}$ | Growth of raindrops by the collection of cloud water | RH83 |
| $P_{RACS}$ | Growth of raindrops by the accretion of snow | RH84 |
| $P_{RAUT}$ | Growth of raindrops by the autoconversion of cloud water | LFO |
| $P_{IDW}$ | Depositional growth of cloud ice from cloud water | KFLC |
| $P_{IACR}$ | Growth of cloud ice by the accretion of rain | RH84 |
| $P_{IHOM}$ | Growth of cloud ice by the homogeneous freezing of cloud water | |
| $P_{DEP}$ | Growth of cloud ice by the deposition of supersaturated vapor | TSM |
| $P_{SAUT}$ | Growth of snow by the conversion of cloud ice | RH83 |
| $P_{SACI}$ | Growth of snow by the collection of cloud ice | RH83 |
| $P_{SACW}$ | Growth of snow by the accretion of cloud water | RH83 |
| $P_{SFW}$ | Growth of snow by the deposition of cloud water | KFLC |
| $P_{SFI}$ | Depositional growth of snow from cloud ice | KFLC |
| $P_{SACR}$ | Growth of snow by the accretion of raindrops | LFO |
| $P_{SDEP}$ | Growth of snow by the deposition of vapor | RH83 |
| $P_{GACI}$ | Growth of graupel by the collection of cloud ice | RH84 |
| $P_{GACR}$ | Growth of graupel by the accretion of raindrops | RH84 |
| $P_{GACS}$ | Growth of graupel by the accretion of snow | RH84 |
| $P_{GACW}$ | Growth of graupel by the accretion of cloud water | RH84 |
| $P_{WACS}$ | Growth of graupel by the riming of snow | RH84 |
| $P_{GDEP}$ | Growth of graupel by the deposition of vapor | RH84 |
| $P_{GFR}$ | Growth of graupel by the freezing of raindrops | LFO |

A 2D framework is used in this study because of the similarities between 2D and 3D model simulations in terms of thermodynamics, surface heat fluxes, rainfall, precipitation efficiency, and vertical transports of mass, sensible heat, and moisture (e.g., Tao and Soong, 1986; Tao et al., 1987; Grabowski et al., 1998; Tompkins, 2000; Khairoutdinov and Randall, 2003; Sui et al., 2005). In addition to the CTL, three sensitivity experiments (NWR, NIR and NCR) are conducted

and compared to study the typhoon rainfall responses to radiation (see Table 2).

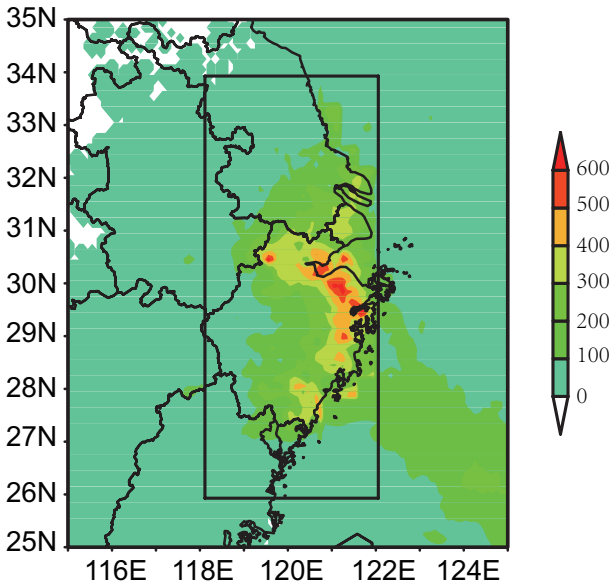


**Fig. 1.** Horizontal distribution of observed rain amount from 5 October to 9 October 2013.

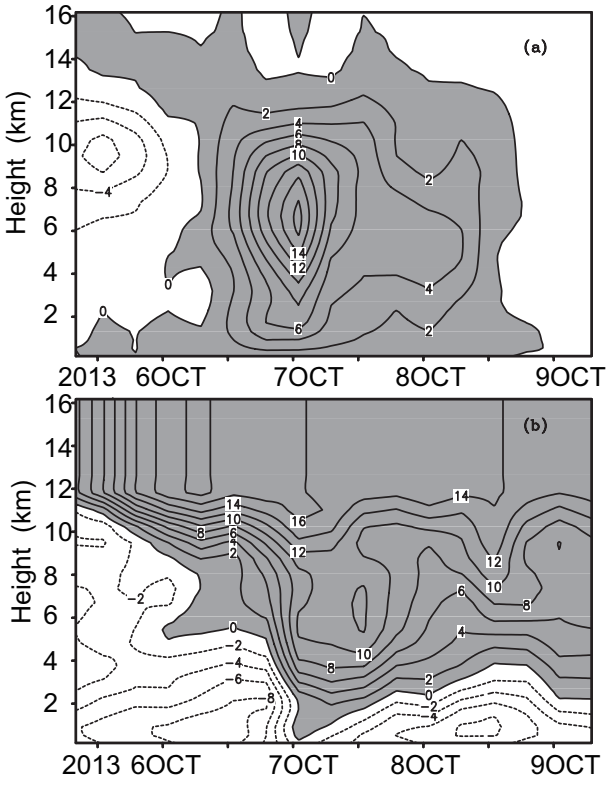


**Fig. 2.** Temporal and vertical distribution of (a) vertical velocity (units: cm $s^{-1}$) and (b) meridional wind (units: m $s^{-1}$) from 0800 LST 5 October to 0800 LST 9 October 2013. Ascending motion in (a) and westerly wind in (b) are shaded. The data are averaged in a rectangular box covering (26°–34°N, 118°–122°E).

**Table 2.** Summary of the (a) experiment designs and (b) differences between experiments.

(a)

| Exp. | Design |
|---|---|
| CTL | Control experiment in which both water and ice hydrometeor mixing ratios are set to non-zero in the calculations of radiation |
| NWR | Water hydrometeor mixing ratios are set to zero in the calculations of radiation |
| NIR | Ice hydrometeor mixing ratios are set to zero in the calculations of radiation |
| NCR | Both water and ice hydrometeor mixing ratios are set to zero in the calculations of radiation |

(b)

| Exp. | Effects to be studied |
|---|---|
| NWR – CTL | Radiative effects of water clouds on rainfall in the presence of radiative effects of ice clouds |
| NCR – NIR | Radiative effects of water clouds on rainfall in the absence of radiative effects of ice clouds |
| NIR – CTL | Radiative effects of ice clouds on rainfall in the presence of radiative effects of water clouds |
| NCR – NWR | Radiative effects of ice clouds on rainfall in the absence of radiative effects of water clouds |

## 3. The control experiment

The evolution of the simulated rain rate averaged over the model domain in CTL is generally similar to that of the observed rain rate averaged over the rectangular box covering (26°–34°N, 118°–122°E) (Fig. 1). The root-mean squared difference (RMSD) between the observed and simulated rain rate in CTL (1.14 mm $h^{-1}$) is significantly smaller than the standard deviation of the observed rain rate (1.84 mm $h^{-1}$). Compared to the observed rain rate, the simulated rain rate shows significant short-term variability (Fig. 3). Li et al. (2002) also revealed a short-term life span (nine hours) of convection in their 2D cloud-resolving model simulation of tropical rainfall. They argued that the short-term life span is attributable to the model physics. The mean simulated rain rate can be analyzed based on the surface rainfall budget (Gao et al., 2005; Cui and Li, 2006):

$$P_S = Q_{WVT} + Q_{WVF} + Q_{WVE} + Q_{CM} \,. \qquad (1)$$

Here, the mean rain rate is associated with drying ($Q_{WVT} > 0$) or moistening ($Q_{WVT} < 0$) of the local atmosphere, water vapor convergence ($Q_{WVF} > 0$) or divergence ($Q_{WVF} < 0$), surface evaporation ($Q_{WVE}$), and cloud hydrometeor loss and convergence ($Q_{CM} > 0$) or gain and divergence ($Q_{CM} < 0$).

The short-term variability of the mean simulated mean rain rate is related to those of the local change in water vapor ($Q_{WVT}$) and clouds ($Q_{CM}$), while water vapor convergence associated with the imposed large-scale vertical velocity largely determines the evolution of the mean rain rate (Fig. 4). The time scale of the variability of $Q_{CM}$ is smaller than that of $Q_{WVT}$. The time scale of the mean rain rate variability

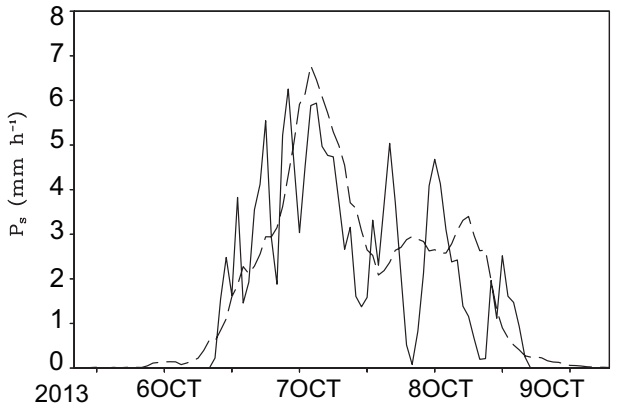


**Fig. 3.** Surface rain rate (units: mm h$^{-1}$) simulated in CTL (solid) and from rain gauge observation (dashed).

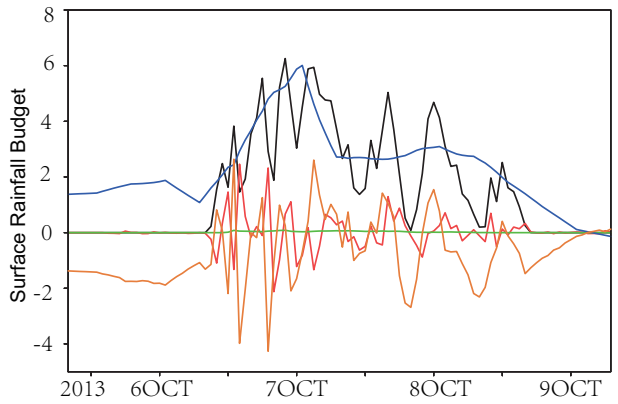


**Fig. 4.** Time series of model domain means of the surface rainfall budget in CTL: $P_S$ (black); $Q_{WVT}$ (orange); $Q_{WVF}$ (blue); $Q_{WVE}$ (green); $Q_{CM}$ (red). Units: mm h$^{-1}$.

corresponds mainly to that of $Q_{WVT}$. Before the occurrence of strong rainfall on 5 October and in the early morning of 6 October, the mean water vapor convergence fails to produce the rainfall because it moistens the local atmosphere, which sets favorable moisture conditions for the development of torrential rainfall later. In the latter part of the day on 8 October and the early part of 9 October, the water vapor convergence decreases rapidly, which leads to the dissipation of strong convection.

The model domain can be categorized into clear-sky, raining stratiform, convective, and non-raining stratiform regions. The area with a total hydrometeor mixing ratio of over $10^{-5}$ g kg$^{-1}$ is considered cloudy. The convective and stratiform rainfall is partitioned using the scheme developed by Tao et al. (1993) and modified by Sui et al. (1994). Over clear-sky regions, water vapor convergence is used to moisten the local atmosphere before the beginning of the rainfall (Fig. 5a). Water vapor divergence generally occurs before the torrential rainfall reaches a maximum at around midnight of 6 October, which leads to drying of the local atmosphere. Water vapor convergence generally occurs after the maximum

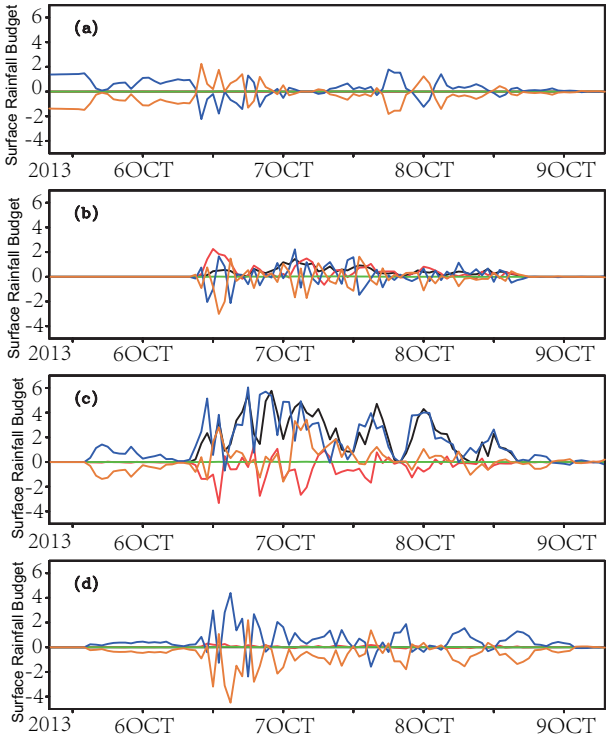


**Fig. 5.** Time series of surface rainfall budget [$P_S$ (black), $Q_{WVT}$ (orange), $Q_{WVF}$ (blue), $Q_{WVE}$ (green) and $Q_{CM}$ (red)] in (a) clear-sky, (b) raining stratiform, (c) convective and (d) non-raining stratiform regions, calculated from CTL. Units: mm h$^{-1}$.

rainfall, which moistens the local atmosphere. Over raining stratiform regions, water vapor convergence, atmospheric drying and hydrometeor convergence are sources of stratiform rainfall (Fig. 5b). Over convective regions, convective rainfall is largely associated with water vapor convergence (Fig. 5c). Over non-raining stratiform regions, water vapor convergence is generally used to increase water vapor in the local atmosphere (Fig. 5d).

## 4. Cloud microphysical and rainfall responses to radiative processes

The RMSDs between the observed and simulated rain rates in NWR (0.87 mm h$^{-1}$), NIR (0.90 mm h$^{-1}$) and NCR (0.94 mm h$^{-1}$) are about 18%–24% smaller than that in CTL (1.14 mm h$^{-1}$). This indicates that the removal of cloud radiative effects leads to better rainfall simulations compared to the observation. The RMSDs may be attributable to the errors from rain gauge observations, the large-scale vertical velocity from the NCEP/GDAS data, and the initial conditions. The reduction in RMSD caused by the exclusion of cloud radiative effects implies that the errors from other model physics, such as the release of latent heat associated with cloud microphysical parameterization schemes and heat divergence, may compensate for the errors from the radiative tendency due to the removal of cloud radiative effects in the thermal balance.

The impacts of radiative processes on cloud microphysics and rainfall are investigated through analysis of four-day and model domain average data. The exclusion of radiative effects of water clouds increases the rain rate from CTL to NWR in the presence of radiative effects of ice clouds, whereas it barely changes the rain rate from NIR to NCR in the absence of radiative effects of ice clouds (Table 3).

To examine the change in cloud processes that are responsible for the change in rainfall, the mean mass-integrated cloud budget is analyzed. The cloud budget is expressed by

$$P_S = Q_{NC} + Q_{CM}\,, \tag{2a}$$

$$Q_{NC} = P_{CND} + P_{DEP} + P_{SDEP} + P_{GDEP} - (P_{REVP} + P_{MLTS} + P_{MLTG})\,, \tag{2b}$$

$$Q_{CM} = Q_{CMC} + Q_{CMR} + Q_{CMI} + Q_{CMS} + Q_{CMG}. \tag{2c}$$

Here, $Q_{NC}$ is the net condensation, and the cloud microphysical terms on the right-hand side of Eq. (2b) can be found in Table 1. The mean hydrometeor change ($Q_{CM}$) can be broken down into the mean hydrometeor change in cloud water ($Q_{CMC}$), raindrops ($Q_{CMR}$), cloud ice ($Q_{CMI}$), snow ($Q_{CMS}$), and graupel ($Q_{CMG}$).

The increase in the rain rate from CTL to NWR is associated with the enhancement in hydrometeor loss, while the net condensation rates are similar in the two experiments. The similar rain rate in NIR and NCR corresponds to similar net condensation and hydrometeor loss.

The similar net condensation rates in CTL and NWR, and in NIR and NCR, are related to the offset between the increases in the vapor condensation ($P_{CND}$) and evaporation of rain ($P_{REVP}$) (Table 4). The increase in hydrometeor loss from CTL to NWR corresponds to the change in graupel from a gain in CTL to a loss in NWR (Table 5), which corresponds mainly to the decrease in accretion of raindrops by cloud ice ($P_{IACR}$) (Table 6). The reduction in $P_{IACR}$ may be related to the decrease in cloud ice, which corresponds to the weakened vapor deposition ($P_{DEP}$) as a result of the increase in saturation specific humidity associated with suppressed infrared radiative cooling at around 6–10 km (Fig. 6). Note that the difference in radiative tendency is determined by the

**Table 3.** Cloud microphysical budgets ($P_S$, $Q_{NC}$, and $Q_{CM}$) averaged for four days over the model domain and their RI and FRC (a) in CTL, NWR, NIR and NCR, and (b) their differences (NWR – CTL, NCR – NIR, NIR – CTL and NCR – NWR). Units are mm d$^{-1}$ for the cloud microphysical budget and RI, and % for FRC.

(a)

| | CTL | NWR | NIR | NCR |
|---|---|---|---|---|
| $P_S$ | 38.28 | 39.67 | 40.68 | 40.66 |
| $Q_{NC}$ | 37.80 | 37.68 | 39.23 | 39.06 |
| $Q_{CM}$ | 0.48 | 1.99 | 1.45 | 1.60 |
| RI | 184.80 | 199.12 | 231.01 | 207.45 |
| FRC | 20.71 | 19.92 | 17.61 | 19.60 |

(b)

| | NWR – CTL | NCR – NIR | NIR – CTL | NCR – NWR |
|---|---|---|---|---|
| $P_S$ | 1.39 | −0.02 | 2.40 | 0.99 |
| $Q_{NC}$ | −0.12 | −0.17 | 1.43 | 1.38 |
| $Q_{CM}$ | 1.51 | 0.15 | 0.97 | −0.39 |
| RI | 14.32 | −23.56 | 46.21 | 8.33 |
| FRC | −0.79 | 1.99 | −3.10 | −0.32 |

**Table 4.** Breakdown of $Q_{NC}$ into $P_{CND}$, $P_{DEP}$, $P_{SDEP}$, $P_{GDEP}$, $-P_{REVP}$, $-P_{MLTS}$ and $-P_{MLTG}$ averaged over the model domain and four days (a) in CTL, NWR, NIR and NCR, and (b) their differences (NWR – CTL, NCR – NIR, NIR – CTL and NCR – NWR). Units: mm d$^{-1}$.

(a)

| | CTL | NWR | NIR | NCR |
|---|---|---|---|---|
| $Q_{NC}$ | 37.80 | 37.68 | 39.23 | 39.06 |
| $P_{CND}$ | 48.71 | 50.02 | 49.94 | 52.20 |
| $P_{DEP}$ | 4.51 | 4.40 | 4.49 | 4.40 |
| $P_{SDEP}$ | 0.64 | 0.71 | 0.62 | 0.67 |
| $P_{GDEP}$ | 0.73 | 0.75 | 0.76 | 0.75 |
| $-P_{REVP}$ | −15.80 | −17.07 | −15.52 | −17.66 |
| $-P_{MLTS}$ | −0.03 | −0.02 | −0.03 | −0.03 |
| $-P_{MLTG}$ | −0.96 | −1.11 | −1.03 | −1.27 |

(b)

| | NWR – CTL | NCR – NIR | NIR – CTL | NCR – NWR |
|---|---|---|---|---|
| $Q_{NC}$ | −0.12 | −0.17 | 1.43 | 1.38 |
| $P_{CND}$ | 1.31 | 2.26 | 1.23 | 2.18 |
| $P_{DEP}$ | −0.11 | −0.09 | −0.02 | 0.00 |
| $P_{SDEP}$ | 0.07 | 0.05 | −0.02 | −0.04 |
| $P_{GDEP}$ | 0.02 | −0.01 | 0.03 | 0.00 |
| $-P_{REVP}$ | −1.27 | −2.14 | −0.28 | −0.59 |
| $-P_{MLTS}$ | 0.01 | 0.00 | 0.00 | −0.01 |
| $-P_{MLTG}$ | −0.15 | −0.24 | 0.07 | −0.16 |

**Table 5.** (a) Breakdown of $Q_{CM}$ into $Q_{CMC}$, $Q_{CMR}$, $Q_{CMI}$, $Q_{CMS}$ and $Q_{CMG}$ in CTL, NWR, NIR and NCR, and (b) their difference for NWR – CTL and NCR – NIR. Units: mm d$^{-1}$.

(a)

| | CTL | NWR | NIR | NCR |
|---|---|---|---|---|
| $Q_{CM}$ | 0.48 | 1.99 | 1.45 | 1.60 |
| $Q_{CMC}$ | 0.17 | −0.30 | −0.14 | 0.51 |
| $Q_{CMR}$ | 1.38 | 0.34 | 2.00 | 0.73 |
| $Q_{CMI}$ | 0.04 | 0.14 | 0.10 | −0.04 |
| $Q_{CMS}$ | −0.59 | 0.06 | −0.04 | 0.94 |
| $Q_{CMG}$ | −0.54 | 1.76 | −0.46 | −0.53 |

(b)

| | NWR – CTL | NCR – NIR | NIR – CTL | NCR – NWR |
|---|---|---|---|---|
| $Q_{CM}$ | 1.51 | 0.15 | 0.97 | −0.39 |
| $Q_{CMC}$ | −0.47 | 0.65 | −0.31 | 0.81 |
| $Q_{CMR}$ | −1.04 | −1.27 | 0.62 | 0.39 |
| $Q_{CMI}$ | 0.10 | −0.14 | 0.06 | −0.18 |
| $Q_{CMS}$ | 0.65 | 0.98 | 0.55 | 0.88 |
| $Q_{CMG}$ | 2.3 | −0.07 | 0.08 | −2.29 |

**Table 6.** Four-day mean $Q_{CMG}$ (units: mm d$^{-1}$) in CTL and NWR and their difference for NWR − CTL. $Q_{CMG} = -P_{GACI}(T < T_o) - P_{GACW}(T < T_o) - P_{GACS} - P_{LACR}(T < T_o) - P_{GACR}(T < T_o) - P_{WACS}(T < T_o) + P_{GMLT}(T > T_o) - P_{GDEP}(T < T_o) + P_{MLTG}(T > T_o)$.($T_o$=0°C)

| | CTL | NWR | NWR − CTL |
|---|---|---|---|
| $Q_{CMG}$ | −0.54 | 1.76 | 2.30 |
| $-P_{GACI}$ | −0.26 | −0.22 | 0.02 |
| $-P_{GACW}$ | −8.77 | −8.28 | 0.49 |
| $-P_{GACS}$ | −4.97 | −5.18 | −0.21 |
| $-P_{IACR}$ | −1.47 | −0.40 | 1.07 |
| $-P_{GACR}$ | −0.53 | −0.29 | 0.24 |
| $-P_{WACS}$ | −1.35 | −1.16 | 0.19 |
| $P_{GMLT}$ | 16.72 | 17.03 | 0.31 |
| $-P_{GDEP}$ | −0.73 | −0.75 | −0.02 |
| $P_{MLTG}$ | 0.96 | 1.11 | 0.15 |

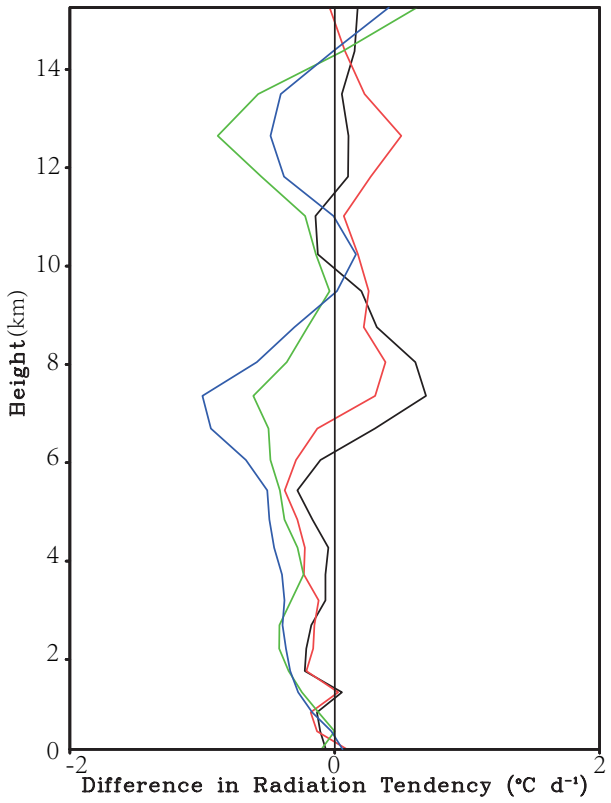


**Fig. 6.** Vertical profiles of difference in radiation tendency for NWR − CTL (black), NCR − NIR (red), NIR − CTL (green), and NCR − NWR (blue), averaged over four days. Units: °C d$^{-1}$.

difference in infrared radiative cooling because the difference in solar radiative heating is generally much smaller than the difference in infrared radiative cooling (not shown). Compared to CTL, The removal of radiative effects of water cloud in NWR allows radiation emitted from the lower troposphere to reach the bottom of ice clouds, and the radiative effects of ice clouds trap radiation to suppress the infrared radiative cooling in the mid and upper troposphere from CTL to NWR.

The similar hydrometeor loss in NIR and NCR is due to the fact that the changes in cloud water and snow from a gain in NIR to a loss in NCR are mainly balanced by the decrease in raindrop loss. The changes in cloud water and snow from a gain in NIR to a loss in NCR are mainly associated with the increase in the collection of cloud water by rain ($P_{RACW}$) and accretion of snow by graupel ($P_{GACS}$), respectively (Tables 7 and 8). The decrease in raindrop loss from NIR to NCR is related to the reduction in rain source through the increase in $P_{RACW}$ (Table 9). The increase in $P_{RACW}$ corresponds to enhanced vapor condensation ($P_{CND}$) through the reduction in saturation specific humidity associated with the enhanced infrared radiative cooling from NIR to NCR in the lower troposphere (Fig. 6). The increase in $P_{GACS}$ is related to the increase in snow, while graupel decreases from NIR to NCR. The increase in snow is related to the increased snow source from the accretion of cloud water ($P_{SACW}$) and raindrops ($P_{SACR}$) by snow through the increases in cloud water and raindrops associated with the increase in $P_{CND}$. Although radiative effects of ice clouds are excluded in both NIR and NCR, water vapor traps the radiation emitted from the lower troposphere in NCR to slightly weaken infrared radiative cooling in the upper troposphere from NIR to NCR.

**Table 7.** Four-day mean $Q_{CMC}$ (units: mm d$^{-1}$) in NIR and NCR and their difference for NCR − NIR. $Q_{CMC} = P_{SACW} + P_{RAUT} + P_{RACW} + P_{GACW} - P_{CND} + P_{IHOM}(T < T_{oo})$. ($T_{oo}$=−35°C).

| | NIR | NCR | NCR − NIR |
|---|---|---|---|
| $Q_{CMC}$ | −0.14 | 0.51 | 0.65 |
| $P_{SACW}$ | 1.37 | 1.47 | 0.10 |
| $P_{RAUT}$ | 0.63 | 0.69 | 0.06 |
| $P_{RACW}$ | 37.07 | 39.92 | 2.85 |
| $P_{GACW}$ | 10.50 | 10.38 | −0.12 |
| $-P_{CND}$ | −49.94 | −52.20 | −2.26 |
| $P_{IHOM}$ | 0.05 | 0.09 | 0.04 |

**Table 8.** Four-day mean $Q_{CMS}$ (units: mm d$^{-1}$) in NIR and NCR and their difference for NCR − NIR. $Q_{CMS} = -P_{SAUT}(T < T_o) - P_{SACI}(T < T_o) - P_{SACW}(T < T_o) - P_{SFI}(T < T_o) + P_{RACS}(T > T_o) + P_{GACS} + P_{SMLT}(T > T_o) - P_{SACR}(T < T_o) - P_{SDEP}(T < T_o) + P_{WACS}(T < T_o)$.

| | NIR | NCR | NCR − NIR |
|---|---|---|---|
| $Q_{CMS}$ | −0.04 | 0.94 | 0.98 |
| $-P_{SAUT}$ | −3.42 | −3.35 | 0.07 |
| $-P_{SACI}$ | −0.12 | −0.11 | 0.01 |
| $-P_{SACW}$ | −1.37 | −1.47 | −0.10 |
| $-P_{SFI}$ | −0.80 | −0.77 | 0.03 |
| $P_{RACS}$ | 0.17 | 0.17 | 0.00 |
| $P_{GACS}$ | 5.22 | 6.41 | 1.19 |
| $P_{SMLT}$ | 0.30 | 0.44 | 0.14 |
| $P_{SACR}$ | −0.59 | −0.68 | −0.09 |
| $-P_{SDEP}$ | −0.62 | −0.67 | −0.05 |
| $P_{WACS}$ | 1.30 | 1.07 | −0.23 |

**Table 9.** Four-day mean $Q_{CMR}$ (units: mm d$^{-1}$) in NIR and NCR and their difference for NCR − NIR. $Q_{CMR} = -P_{RAUT} - P_{RACW} - P_{GACW}(T > T_o) + P_{REVP} - P_{RACS}(T > T_o) + P_{LACR}(T < T_o) + P_{GACR}(T < T_o) - P_{SMLT}(T > T_o) - P_{GMLT}(T > T_o) + P_S$.

| | NIR | NCR | NCR − NIR |
|---|---|---|---|
| $Q_{CMR}$ | 2.00 | 0.73 | −1.27 |
| $-P_{RAUT}$ | −0.63 | −0.69 | −0.06 |
| $-P_{RACW}$ | −37.07 | −39.92 | −2.85 |
| $-P_{GACW}$ | −1.32 | −1.36 | −0.04 |
| $P_{REVP}$ | 15.52 | 17.66 | 2.14 |
| $-P_{RACS}$ | −0.17 | −0.17 | 0.00 |
| $P_{IACR}$ | 0.90 | 1.15 | 0.25 |
| $P_{GACR}$ | 0.90 | 0.46 | −0.44 |
| $-P_{SMLT}$ | −0.30 | −0.44 | −0.14 |
| $-P_{GMLT}$ | −17.20 | −17.38 | −0.18 |
| $P_S$ | 40.68 | 40.66 | −0.02 |

The removal of radiative effects of ice clouds strengthens the rain rate primarily through the increases in net condensation from CTL to NIR and NWR to NCR (Table 3). The enhancement in net condensation corresponds to the increase in $P_{CND}$ (Table 4) through the decrease in saturation specific humidity associated with the enhanced infrared radiative cooling from CTL to NIR and NWR to NCR (Fig. 6) caused primarily by the exclusion of radiative effects of ice clouds. Compared to NWR, the removal of the effects of water clouds in NCR makes atmospheric layers more transparent to the radiation emitted from the lower troposphere and leads to more radiation escaping. As a result, the enhancement in infrared radiative cooling from NWR to NCR is stronger than that from NIR to CTL.

The enhancement in rainfall decreases from NIR − CTL to NCR − NWR through the change from the increase in hydrometeor loss for NIR − CTL to the decrease in hydrometeor loss for NCR − NWR (Table 3). The increase in rainfall dramatically reduces from NWR − CTL to NCR − NIR via the slowdown in the enhanced hydrometeor loss. These results correspond primarily to the decrease in $P_{IACR}$ from CTL to NWR, while the decrease in $P_{IACR}$ from NIR to NCR is relatively small (Table 5). The reduction in $P_{IACR}$ from CTL to NWR is associated with the suppressed infrared radiative cooling (Fig. 6).

Ping et al. (2011) conducted a similar set of sensitivity experiments to those performed in this study but, in their experiments, zero large-scale vertical velocity and height-invariant zonal wind and time-invariant sea surface temperature were imposed in the model during the equilibrium integrations. The similarity between the two studies is that rainfall increases when radiative effects of water clouds are excluded in the presence of radiative effects of ice clouds, or when radiative effects of ice clouds are removed [see Table 3 in this study and Table 2 in Ping et al. (2011)]. The difference between the two studies is that in the absence of radiative effects of ice clouds, rainfall is insensitive to radiative effects of water clouds in this study, whereas rainfall increases when radiative effects of water clouds are eliminated in Ping et al. (2011).

Following Li et al. (2015), the model domain mean rain rate is a product of RI (rain rate average over the rainfall area) and FRC (the ratio of rain grids to total model domain grids), i.e.,

$$P_S = \mathrm{RI} \times \mathrm{FRC}. \tag{3}$$

Like the aforementioned model domain rainfall responses to radiative processes, the exclusion of radiative effects of water clouds increases the RI from CTL to NWR (Table 3). The removal of radiative effects of ice clouds increases the RI from CTL to NIR and from NWR to NCR. Unlike the radiative effects of water clouds on rainfall from NIR to NCR, the elimination of radiative effects of water clouds decreases the RI from NIR to NCR. The FRC reduces from CTL to NWR, and from CTL to NIR and NWR to NCR, whereas it increases from NIR to NCR.

Li et al. (2014) defined the maximum rain rate as the sum of (1) local atmospheric drying and (2) water and hydrometeor convergence, based on rainfall separation via the surface rainfall budget. We calculated the mean cloud microphysical budget and RI and FRC associated with the maximum rainfall, and their responses to radiative processes (Table 10). The mean rainfall increases from CTL to NWR, and from CTL to NIR, mainly through the enhanced net condensation; whereas, it reduces from NIR to NCR, and from NWR to NCR, via the suppressed net condensation. In contrast, the exclusion of radiative effects decreases the maximum RI regardless of water or ice clouds.

Based on Eq. (3), the difference in $P_S(y)$ and $P_S(x)$ can be written as

$$\begin{aligned} P_S(y) - P_S(x) &= \mathrm{RI}(y)\mathrm{FRC}(y) - \mathrm{RI}(x)\mathrm{FRC}(x) \\ &= [\mathrm{RI}(y) - \mathrm{RI}(x)][\mathrm{FRC}(y) - \mathrm{FRC}(x)] + \\ &\quad \mathrm{RI}(x)[\mathrm{FRC}(y) - \mathrm{FRC}(x)] + \\ &\quad \mathrm{FRC}(x)[\mathrm{RI}(y) - \mathrm{RI}(x)]. \end{aligned} \tag{4}$$

Here, $(y,x) = (\mathrm{NWR},\mathrm{CTL}), (\mathrm{NCR},\mathrm{NIR}), (\mathrm{NIR},\mathrm{CTL}), (\mathrm{NCR},\mathrm{NWR})$. Table 11a shows that $P_S(y) - P_S(x)$ is controlled

**Table 10.** As in Table 3 but for those associated with maximum rainfall.

(a)

| | CTL | NWR | NIR | NCR |
|---|---|---|---|---|
| $P_S$ | 3.46 | 4.18 | 4.41 | 3.93 |
| $Q_{NC}$ | 2.03 | 2.54 | 2.74 | 2.31 |
| $Q_{CM}$ | 1.43 | 1.64 | 1.67 | 1.61 |
| RI | 1718.41 | 1632.54 | 1669.11 | 1621.24 |
| FRC | 0.201 | 0.256 | 0.264 | 0.242 |

(b)

| | NWR − CTL | NCR − NIR | NIR − CTL | NCR − NWR |
|---|---|---|---|---|
| $P_S$ | 0.72 | −0.48 | 0.95 | −0.25 |
| $Q_{NC}$ | 0.51 | −0.43 | 0.71 | −0.23 |
| $Q_{CM}$ | 0.21 | −0.06 | 0.24 | −0.003 |
| RI | −85.87 | −47.87 | −49.30 | −11.30 |
| FRC | 0.055 | −0.022 | 0.053 | −0.014 |

**Table 11.** Differences in (a) domain mean rain rate and (b) maximum rain rate for NWR − CTL, NCR − NIR, NIR − CTL and NCR − NWR, and their relationships to differences in RI and FRC. $P_{S1} = [\mathrm{RI}(y) - \mathrm{RI}(x)][\mathrm{FRC}(y) - \mathrm{FRC}(x)]$, $P_{S2} = \mathrm{RI}(x)[\mathrm{FRC}(y) - \mathrm{FRC}(x)]$, $P_{S3} = \mathrm{FRC}(x)[\mathrm{RI}(y) - \mathrm{RI}(x)]$. Units: mm $\mathrm{d}^{-1}$.

(a)

| | NWR − CTL | NCR − NIR | NIR − CTL | NCR − NWR |
|---|---|---|---|---|
| $P_S$ | 1.39 | −0.02 | 2.40 | 0.99 |
| $P_{S1}$ | −0.11 | −0.47 | −1.44 | −0.08 |
| $P_{S2}$ | −1.46 | 4.60 | −5.97 | −0.64 |
| $P_{S3}$ | 2.96 | −4.15 | 9.81 | 1.71 |

(b)

| | NWR − CTL | NCR − NIR | NIR − CTL | NCR − NWR |
|---|---|---|---|---|
| $P_S$ | 0.72 | −0.48 | 0.95 | −0.25 |
| $P_{S1}$ | −0.05 | 0.01 | −0.03 | 0.00 |
| $P_{S2}$ | 0.95 | −0.37 | 0.91 | −0.23 |
| $P_{S3}$ | −0.18 | −0.12 | 0.07 | −0.02 |

by $\mathrm{FRC}(x)[\mathrm{RI}(y) - \mathrm{RI}(x)]$. This suggests that cloud radiative effects on model domain mean rainfall is interrelated with cloud radiative effects on RI. For maximum rainfall, $P_S(y) - P_S(x)$ is determined by $\mathrm{RI}(x)[\mathrm{FRC}(y) - \mathrm{FRC}(x)]$ (Table 11b). This indicates that cloud radiative effects on model domain mean maximum rainfall correspond to cloud radiative effects on the fractional coverage of maximum rainfall.

## 5. Summary

Cloud-resolving model sensitivity experiments of Typhoon Fitow (2013) were conducted to study the cloud microphysical and rainfall responses to radiative processes during the typhoon's landfall. The rain rate simulated in CTL was compared with observed rain gauge data. The analysis of the RMSD between simulation and observation, and the standard deviation, showed fair agreement between the simulation and observation. The comparison of the model domain mean cloud budget between the sensitivity experiments revealed that the exclusion of radiative effects of water clouds increases the mean rainfall through the enhanced hydrometeor loss caused by the decrease in accretion of raindrops by cloud ice in the presence of radiative effects of ice clouds; whereas, it barely changes rainfall in the absence of radiative effects of ice clouds. The removal of radiative effects of ice clouds increases the mean rainfall through the strengthened net condensation regardless of the radiative effects of water clouds. The difference in model domain mean rain rate caused by cloud radiative effects is related to the difference in RI.

The increases in maximum rainfall are associated with the exclusion of radiative effects of water clouds in the presence of radiative effects of ice clouds, or the removal of radiative effects of ice clouds in the presence of radiative effects of water clouds, mainly through the enhancements in net condensation. The decreases in maximum rainfall correspond to the elimination of radiative effects of water clouds in the absence of radiative effects of ice clouds, or the removal of radiative effects of ice clouds in the absence of radiative effects of water clouds, through the reductions in net condensation. The difference in the maximum rain rate caused by cloud radiative effects is related to the difference in the fractional coverage of maximum rainfall.

***Acknowledgements.*** The authors thank Dr. W.-K. TAO at NASA/GSFC for his cloud-resolving model, and the Editor (Dr. Z. SUN) and the two reviewers for their constructive comments. This work was supported by the National Natural Science Foundation of China (Grant No. 41475039) and the National Key Basic Research and Development Project of China (Grant No. 2015CB953601).

### REFERENCES

Chou, M.-D., 1992: A solar radiation model for use in climate studies. *J. Atmos. Sci.*, **49**, 762–772.

Chou, M.-D., and M. J. Suarez, 1994: An efficient thermal infrared radiation parameterization for use in general circulation model. NASA Tech. Memo. 104606, Vol. 3, 85 pp. [Available from NASA/Goddard Space Flight Center, Code 913, Greenbelt, MD 20771.]

Chou, M. D., D. P. Kratz, and W. Ridgway, 1991: Infrared radiation parameterizations in numerical climate models. *J. Climate*, **4**, 424–437.

Chou, M. D., M. J. Suarez, C. H. Ho, M. M. H. Yan, and K. T. Lee, 1998: Parameterizations for cloud overlapping and shortwave single-scattering properties for use in general circulation and cloud ensemble models. *J. Climate*, **11**, 202–214.

Cui, X. P., and X. F. Li, 2006: Role of surface evaporation in surface rainfall processes. *J. Geophys. Res.*, **111**, D17112, doi: 10.1029/2005JD006876.

Dudhia, J., 1989: Numerical study of convection observed during the winter monsoon experiment using a mesoscale two-dimensional model. *J. Atmos. Sci.*, **46**, 3077–3107.

Gao, S. T., and X. F. Li, 2008: *Cloud-resolving Modeling of Convective Processes*. Springer, Dordrecht, 206 pp.

Gao, S. T., and X. F. Li, 2010: Precipitation equations and their applications to the analysis of diurnal variation of tropical oceanic rainfall. *J. Geophys. Res.*, **115**, D08204, doi: 10.1029/2009JD012452.

Gao, S. T., X. P. Cui, Y. S. Zhou, and X. F. Li, 2005: Surface rainfall processes as simulated in a cloud-resolving model. *J. Geophys. Res.*, **110**, D10202, doi: 10.1029/2004JD005467.

Gao, S. T., X. P. Cui, and X. F. Li, 2009: A modeling study of diurnal rainfall variations during the 21-day period of TOGA COARE. *Adv. Atmos. Sci.*, **26**, 895–905, doi: 10.1007/s00376-009-8123-6.

Grabowski, W. W., X. Q. Wu, M. W. Moncrieff, and W. D. Hall, 1998: Cloud-resolving model of tropical cloud systems during Phase III of GATE. Part II: Effects of resolution and the third spatial dimension. *J. Atmos. Sci.*, **55**, 3264–3282.

Gray, W. M., and R. W. Jacobson Jr., 1977: Diurnal variation of deep cumulus convection. *Mon. Wea. Rev.*, **105**, 1171–1188.

Khairoutdinov, M. F., and D. A. Randall, 2003: Cloud-resolving modeling of the ARM summer 1997 IOP: Model formulation, results, uncertainties, and sensitivities. *J. Atmos. Sci.*, **60**, 607–625.

Krueger, S. K., Q. Fu, K. N. Liou, and H.-N. S. Chin, 1995: Improvement of an ice-phase microphysics parameterization for use in numerical simulations of tropical convection. *J. Appl. Meteor.*, **34**, 281–287.

Li, X. F., and S. T. Gao, 2011: *Precipitation Modeling and Quantitative Analysis*. Springer, Dordrecht, 240 pp.

Li, X. F., C.-H. Sui, K.-M. Lau, and M.-D. Chou, 1999: Large-scale forcing and cloud-radiation interaction in the tropical deep convective regime. *J. Atmos. Sci*., **56**, 3028–3042.

Li, X. F., C.-H. Sui, and K.-M. Lau, 2002: Dominant cloud microphysical processes in a tropical oceanic convective system: A 2-D cloud resolving modeling study. *Mon. Wea. Rev.*, **130**, 2481–2491.

Li, X. F., G. Q. Zhai, S. T. Gao, and X. Y. Shen, 2014: A new convective-stratiform rainfall separation scheme. *Atmos. Sci. Lett.*, **15**, 245–251.

Li, X. F., G. Q. Zhai, P. J. Zhu, and R. Liu, 2015: An equilibrium cloud-resolving modeling study of diurnal variation of tropical rainfall. *Dyn. Atmos. Ocean*, **71**, 108–117.

Lilly, D. K., 1988: Cirrus outflow dynamics. *J. Atmos. Sci.*, **45**, 1594–1605.

Lin, Y.-L., R. D. Farley, and H. D. Orville, 1983: Bulk parameterization of the snow field in a cloud model. *J. Climate Appl. Meteor*., **22**, 1065–1092.

Ping, F., Z. Luo, and H. Wang, 2011: Effects of ice and water clouds on rainfall: A partitioning analysis based on surface rainfall budget. *Atmos. Sci. Lett.*, **12**, 300-308.

Rutledge, S. A., and P. V. Hobbs, 1983: The mesoscale and microscale structure and organization of clouds and precipitation in midlatitude cyclones. Part VIII: A model for the "seeder-feeder" process in warm-frontal rainbands. *J. Atmos. Sci*., **40**, 1185–1206.

Rutledge, S. A., and P. V. Hobbs, 1984: The mesoscale and microscale structure and organization of clouds and precipitation in midlatitude cyclones. Part XII: A diagnostic modeling study of precipitation development in narrow cold-frontal rainbands. *J. Atmos. Sci*., **41**, 2949–2972.

Soong, S. T., and Y. Ogura, 1980: Response of tradewind cumuli to large-scale processes. *J. Atmos. Sci.*, **37**, 2035–2050.

Soong, S. T., and W.-K. Tao, 1980: Response of deep tropical cumulus clouds to Mesoscale processes. *J. Atmos. Sci.*, **37**, 2016–2034.

Sui, C.-H., K.-M. Lau, W.-K. Tao, and J. Simpson, 1994: The tropical water and energy cycles in a cumulus ensemble model. Part I: Equilibrium climate. *J. Atmos. Sci*., **51**, 711–728.

Sui, C.-H., K.-M. Lau, Y. N. Takayabu, and D. Short, 1997: Diurnal variations in tropical oceanic cumulus convection during TOGA COARE. *J. Atmos. Sci*., **54**, 639–655.

Sui, C.-H., X. Li, and K.-M. Lau, 1998: Radiative-convective processes in simulated diurnal variations of tropical oceanic convection. *J. Atmos. Sci*., **55**, 2345–2359.

Sui, C.-H., X. F. Li, M.-J. Yang, and H.-L. Huang, 2005: Estimation of oceanic precipitation efficiency in cloud models. *J. Atmos. Sci.*, **62**, 4358–4370.

Tao, W. K., and S. T. Soong, 1986: A study of the response of deep tropical clouds to mesoscale processes: Three-dimensional numerical experiments. *J. Atmos. Sci.*, **43**, 2653–2676.

Tao, W.-K., and J. Simpson, 1993: The Goddard Cumulus Ensemble model. Part I: Model description. *Terrestrial Atmospheric and Oceanic Sciences*, **4**, 35–72.

Tao, W.-K., J. Simpson, and S.-T. Soong, 1987: Statistical properties of a cloud ensemble: A numerical study. *J. Atmos. Sci.*, **44**, 3175–3187.

Tao, W.-K, J. Simpson, and M. McCumber, 1989: An ice-water saturation adjustment. *Mon. Wea. Rev.*, **117**, 231–235.

Tao, W. K., J. Simpson, C. H. Sui, B. Ferrier, S. Lang, J. Scala, M. D. Chou, and K. Pickering, 1993: Heating, moisture, and water budgets of tropical and midlatitude squall lines: Comparisons and sensitivity to longwave radiation. *J. Atmos. Sci.*, **50**, 673–690.

Tompkins, A. M., 2000: The impact of dimensionality on long-term cloud-resolving model simulations. *Mon. Wea. Rev.*, **128**, 1521–1535.